

# A temperature dependent measurement of the carrier velocity vs. electric field characteristic for as-grown and H-intercalated epitaxial graphene on SiC

M. Winters,<sup>1</sup> J. Hassan,<sup>2</sup> H. Zirath,<sup>1</sup> E. Janzén,<sup>2</sup> and N. Rorsman<sup>1</sup>

<sup>1</sup>*Department of Microtechnology and Nanoscience, Chalmers University of Technology, Kemivägen 9, 412 96 Göteborg, Sweden*

<sup>2</sup>*Department of Physics, Chemistry and Biology (IFM), Linköping University, Linköping, Sweden*

(Received 3 April 2013; accepted 2 May 2013; published online 20 May 2013)

A technique for the measurement of the electron velocity versus electric field is demonstrated on as-grown and H-intercalated graphene. Van der Pauw, coplanar microbridge, and coplanar TLM structures are fabricated in order to assess the carrier mobility, carrier concentration, sheet resistance, and contact resistance of both epi-materials. These measurements are then combined with dynamic IV measurements to extract a velocity-field characteristic. The saturated electron velocity measurements indicate a value of  $2.33 \times 10^7$  cm/s for the as-grown material and  $1.36 \times 10^7$  cm/s for the H-intercalated material at 300 K. Measurements are taken as a function of temperature from 100 K to 325 K in order to estimate the optical phonon energy  $E_{so}$  of 4H-SiC by assuming an impurity scattering model. The extracted values of  $E_{so}$  are 97 meV for the as-grown sample and 115 meV for the H-intercalated sample. The H-intercalated result correlates to the anticipated value of 116 meV for 4H-SiC, while the as-grown value is significantly below the expected value. Therefore, we hypothesize that the transport properties of epitaxial graphene on SiC are influenced both by intercalation and by remote phonon scattering with the SiC substrate.

© 2013 AIP Publishing LLC. [<http://dx.doi.org/10.1063/1.4807162>]

## I. INTRODUCTION

Graphene on SiC has generated a great deal of interest in both the electronics and materials physics community as theoretical calculations and experimental measurements indicate exemplary electronic, mechanical, and thermal properties. Epitaxial graphene on SiC wafers is of particular interest as it potentially provides a route to large scale processing of graphene based devices.

The ability of a device to function at high frequency is limited by the drift velocity ( $v_d$ ) of charge carriers at high-electric fields:  $v_d = \langle \hbar \mathbf{k} \cdot \hat{\mathbf{E}} / m^* \rangle$ . Here,  $m^*$  is the effective mass of the charge carriers,  $\mathbf{k}$  is the wavevector, and  $\hat{\mathbf{E}}$  is the unit vector which points in the direction of the electric field.<sup>1</sup> Drift velocity is limited by scattering events in the material. Carriers in graphene may scatter via impurities, phonons in the substrate, phonons in the graphene, and via Coulomb interactions. The Ensemble Monte Carlo approach is particularly suited to the modelling of carrier scattering in graphene.<sup>1-3</sup>

The most common way to measure the velocity-field characteristic is by a dynamic current voltage measurement. Short pulses are used in order to minimize resistive self heating effects, which may interfere with a proper interpretation of the temperature dependence. This method has been applied to measurements on silicon,<sup>4</sup> silicon carbide,<sup>5</sup> and other materials. Additionally, a capacitive probe method has been used in order to obtain the velocity-field characteristic in semiconductor materials.<sup>6</sup> In another approach, the velocity-field characteristic of GaAs was measured via the injection of electrons into the material with an electron beam.<sup>7</sup> Velocity-field characterization has also been thoroughly explored on graphene on SiO<sub>2</sub> by Dorgan *et al.*<sup>8</sup> An impurity scattering limited saturation velocity of  $>3 \times 10^7$  cm/s is reported for sheet carrier densities

$n < 10^{12}$  cm<sup>-2</sup>. The corresponding optical phonon energy  $E_{OP}$  for SiO<sub>2</sub> is reported to be 56 meV from temperature dependent measurements.

Here, we measure the velocity-field characteristic of graphene to determine potential applications for high-frequency devices. Such a characterization lends valuable physical insight into the transport of charge carriers in two-dimensional structures.<sup>9</sup> As-grown and H-intercalated epitaxial graphenes are prepared on the Si-face of semi-insulating (SI) 4H-SiC wafers with the intention of measuring the field dependence of carrier velocity as a function of temperature. Van der Pauw structures, coplanar transfer length method (TLM) structures, and coplanar microbridge structures are fabricated using standard processing techniques. The Van der Pauw structures are used to motivate an empirical relationship between carrier concentration and sheet resistance. TLM structures are measured to estimate the contact resistance of graphene-metal contacts. Pulsed IV measurements are performed as a function of temperature to obtain an IV characteristic for both materials. These measurements are combined to extract the carrier velocity versus electric field characteristics. These are then fitted to a standard velocity field model in order to determine the saturated electron velocity in both materials.

## II. METHODS

### A. Material growth

Epitaxial graphene was produced by sublimation of carbon in a CVD reactor by heating SiC.<sup>10</sup> Depending on the growth conditions, monolayer, bi-layer, and multilayer graphenes may be formed on the surface of the SiC wafer. However, there are many challenges associated with such an

approach including material uniformity and the existence of a complex terraced substrate surface morphology. A horizontal hot-wall CVD reactor was used for the growth of graphene in vacuum ( $1 \times 10^{-5} - 1 \times 10^{-6}$  mbar) on the Si-face of chemo-mechanically semi-insulating nominally on-axis 4H-SiC substrates. In order to minimize surface degradation in the form of surface step-bunching and defect selective etching on the Si-face, graphene growth was performed at an optimized temperature of 1400 °C.<sup>11</sup> Two sets of samples were grown under the same growth conditions. In one set of samples, only graphene was grown, while the other set of samples was *in situ* intercalated with hydrogen.

The existence of a buffer layer of graphene-like carbon bound to silicon at the SiC/graphene interface has been known for some time.<sup>12</sup> The buffer layer consists of lattice matched  $6\sqrt{3} \times 6\sqrt{3}R30$  carbon atoms with a high density of dangling bonds, which are a result of high temperature processing. Sheet carrier densities in epitaxial graphene tend to be quite high  $10^{12} - 10^{13}$ .<sup>12,13</sup> Hydrogen intercalation converts the interface carbon buffer layer into the first graphene layer and transforms epitaxial graphene into quasi free-standing graphene on the substrate.<sup>12,14</sup> The efficacy of the H-intercalation process may be demonstrated using a variety of techniques such as Raman spectroscopy, SEM, LEEM, XPS, and Angle Resolved Photo Electron Spectroscopy (ARPES). H-intercalated material tends to be p-type with higher carrier concentrations and average carrier mobility, while as-grown material tends to be n-type with lower carrier concentrations and carrier mobility.<sup>14</sup>

## B. Device fabrication

Graphene test structures are produced using standard processing procedures used for semiconductor device fabrication. First, alignment marks are patterned via photolithography, DC sputtering of Ti/Au, and liftoff in acetone. Next, the graphene mesa layer is patterned via photolithography and dry etching in oxygen plasma.<sup>15</sup> The formation of Ohmic contacts is a critical step in the graphene fabrication procedure. The surface is first cleaned using a standard acetone/methanol/isopropyl alcohol (IPA) degreasing. A subsequent cleaning in  $\text{CHCl}_3$  is then performed in order to remove as many organic contaminants and residues from previous processing steps as possible from the surface. Then, Ohmic contacts are patterned using photolithography, DC sputtering of Ti/Au, and liftoff. An additional DC sputtering of Ti/Au and liftoff are done for the formation of contact pads. The contact resistance is measured to be  $2.2 \Omega \text{mm}$  and  $1.2 \Omega \text{mm}$  in as-grown and H-intercalated graphene, respectively. For this extraction, the contact resistance is assumed to be constant over the range of electric field applied to the structure.

Prior to passivation, the samples are annealed in a mixture of atmospheric  $\text{H}_2/\text{Ar}$  in a 1:9 ratio at 300 °C in order to remove residues from previous photolithography steps. Passivation is achieved using a layer of benzocyclobutene (BCB) diluted in [1,3,5] trimethylbenzene in a 1:1 ratio.<sup>16</sup> The BCB layer is spun onto the substrate and then patterned via photolithography. A curing step is performed at 250 °C for 2 h. After curing, the thickness of the BCB passivation layer is  $\sim 2 \mu\text{m}$ . BCB has been selected because it improves

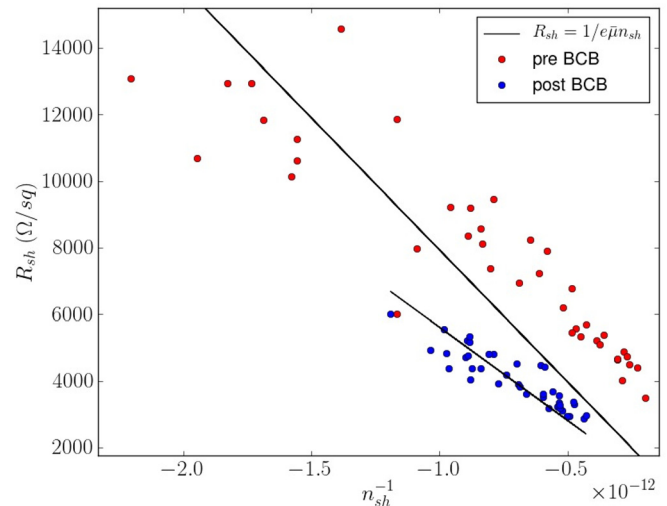


FIG. 1. Plots showing the Hall statistics before and after passivation with BCB for one H-intercalated sample. Statistics are gathered from 40 identical  $100 \mu\text{m} \times 100 \mu\text{m}$  Hall structures fabricated on a single chip.

the large-area uniformity of transport properties. The sheet resistance versus carrier concentration both before and after passivation with BCB demonstrates the positive effects of BCB passivation (Fig. 1). Furthermore, a passivation step is important as ambient  $\text{H}_2\text{O}$  acts as a dopant to graphene.

Velocity-field measurements are performed on  $5 \mu\text{m} \times 10 \mu\text{m}$  microbridge structures (Fig. 2).<sup>5</sup>

## C. Measurement technique

Measurements are carried out using a four part setup consisting of a Tabor 8500A pulse generator, a HP85120A pulse head, an HP6625A two channel supply, and a TDS7104 oscilloscope. Pulse parameters are controlled via a Python script. The pulse generator serves as a clock to generate pulses from the pulse head. The magnitude of the pulse is controlled via setting the voltage on the DC supply, while the pulse width ( $1 \mu\text{s}$ ), rise time (100 ns), and duty cycle

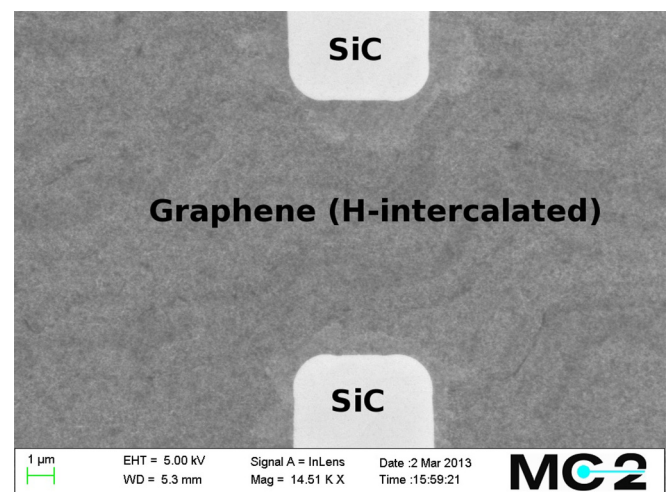


FIG. 2. A SEM image of an H-intercalated graphene microbridge structure used for velocity-field measurements before the fabrication of Ohmic contacts. The image shows the surface morphology of H-intercalated graphene, as well as corner rounding due to photolithography.

(1 ms) are controlled with the pulse generator. Voltage pulses are applied to the microbridge structures, and the output current waveform is measured via a Hall effect probe. The voltage pulses are also monitored using the oscilloscope. The pulse magnitude is swept from 0 V up to the onset of breakdown effects in steps of 1 V. Breakdown effects are observed generally for voltage pulses with  $V > 30$  V. The output current pulse ladder for one measurement is shown in Fig. 3.

The center of a square wave pulse in the time domain may be found using the convolution method.

$$\frac{d}{dt} \left[ \int V(t)V(t-\tau)d\tau \right] = 0,$$

$$\frac{d}{dt} \left[ \int I(t)V(t-\tau)d\tau \right] = 0.$$

The solution to the above equations gives the center of the voltage and current pulses in time ( $t_v$  and  $t_i$ ). The corresponding  $V(t_v)$  and  $I(t_i)$  are taken to be a single point in the IV

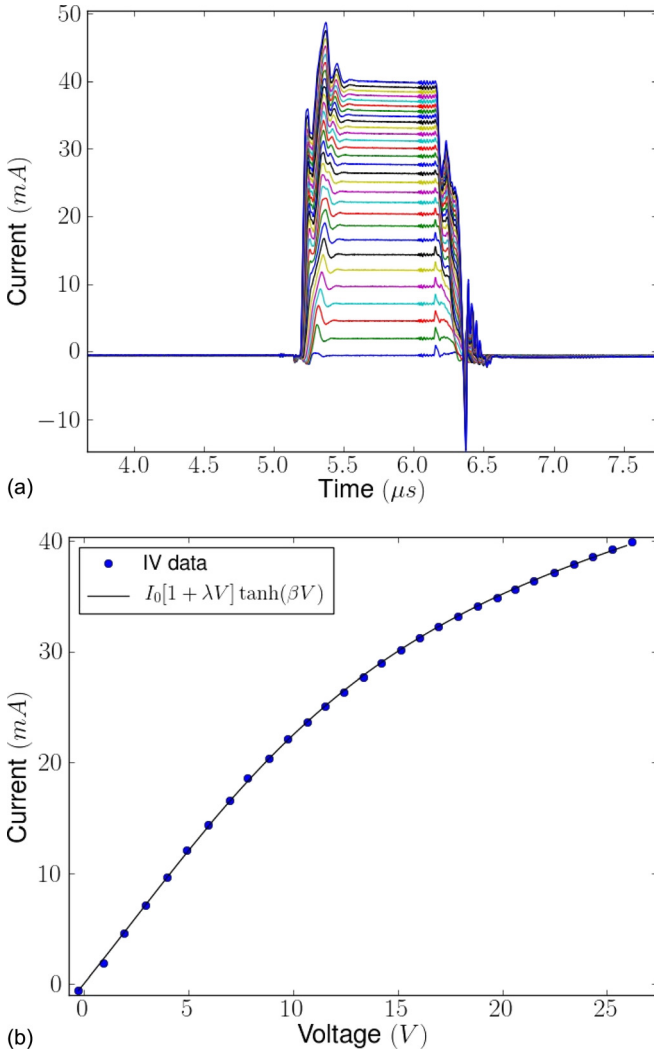


FIG. 3. The current waveform ladder for  $1 \mu\text{s}$  voltage pulses from 0 V to 28 V. (Bottom): The extracted IV characteristic using the convolution method for a fabricated  $5 \mu\text{m} \times 10 \mu\text{m}$  microbridge structure (Fig. 2) after the completion of fabrication. The current spikes in the time domain signals (artifacts from the current probe) are removed from the IV via convolution. The black line represents fitting to Eq. (1).

characteristic. Repeating for all voltage steps gives the full IV characteristic. This method is valid as the current pulses observed are of constant amplitude for each applied voltage. Furthermore, it has the advantage of efficiently finding the correct pulse amplitude in noisy signals.

The following non-linear model may be applied to the extracted IV characteristics with great accuracy.<sup>17</sup>

$$I = I_0[1 + \lambda V]\tanh(\beta V), \quad (1)$$

where  $I_0$  indicates the location of the onset of saturation in the IV characteristic,  $\lambda$  is the channel length modulation parameter, and  $\beta$  is the current saturation parameter.<sup>17</sup> The extracted values from Eq. (1) are  $I_0 = 28.4 \text{ mA}$ ,  $\lambda = 0.0166 \text{ V}^{-1}$ , and  $\beta = 0.0825 \text{ V}^{-1}$  for the IV curve shown in the bottom plot of Fig. 3. Pulsed IV measurements are taken as a function of temperature from  $T = 100 \text{ K}$  to  $T = 325 \text{ K}$  in a closed cycle Helium cryostat under vacuum conditions.

### III. THEORY

A graphene mesa may be considered as a charge carrying sheet. The electron drift velocity may be determined by the following relation:

$$v_d = \frac{I}{en_{sh}w_{ch}}, \quad (2)$$

where  $e$  is the fundamental charge,  $n_{sh}$  is the sheet carrier concentration, and  $w_{ch}$  is the width of the sheet. The determination of the carrier concentration is of fundamental importance for the extraction of the electron velocity from dynamic IV measurements.

The sheet carrier density  $n_{sh}$  is estimated via the sheet resistance  $R_{sh}$ .  $R_{sh}$  is obtained from dynamic IV measurements and knowledge of the geometry of the charge carrying graphene mesa.  $n_{sh}$  may be calculated from  $R_{sh}$  via the following relation:

$$R_{sh} = \frac{1}{en_{sh}\bar{\mu}}. \quad (3)$$

Hall measurements were performed at  $T = 300 \text{ K}$  to obtain the average mobility  $\bar{\mu}$ , allowing for a direct calculation of the carrier density  $n_{sh}$  from the measured low field sheet resistance  $R_{sh}$ . Hall data are used to generate statistics on the relationship between carrier concentration  $n_{sh}$  and sheet resistance  $R_{sh}$ .

On both as-grown and H-intercalated materials, 40 individual  $100 \mu\text{m}^2$  Van der Pauw structures are measured (Fig. 4).<sup>13</sup> The measured Hall data are then fitted to Eq. (3) via a least squares method. Highly asymmetric structures and structures, which have poor Ohmic contacts, were rejected from the data. The result of the fit is the average carrier mobility for the chip ( $\bar{\mu}$ ).

The measured Pearson correlation for fitted Hall data (Fig. 4) is  $\rho = -0.96$  for as-grown material and  $\rho = 0.74$  for H-intercalated material after the deposition of passivation. The average mobility ( $\bar{\mu}$ ) for the as-grown material is  $877 \text{ cm}^2/\text{V s}$  and the H-intercalated material is  $1042 \text{ cm}^2/\text{V s}$ . These values agree with microwave reflectivity measurements

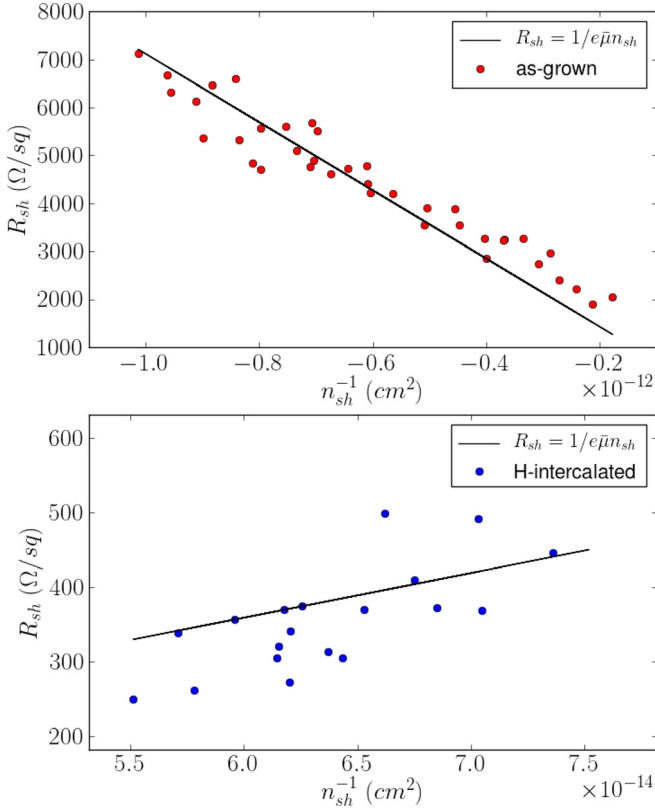


FIG. 4. A plot showing the measured carrier density versus sheet resistance from Hall mobility data. The data were extracted from 40 identical Hall structures fabricated on both as-grown and H-intercalated material, respectively, and fitted to Eq. (3).

of the mobility, which give  $835 \text{ cm}^2/\text{Vs}$  for the as-grown material and  $1143 \text{ cm}^2/\text{Vs}$  for H-intercalated material. The microwave reflectivity measurements are performed after material growth and prior to any fabrication of devices. The distribution of the measured mobility data for both materials is shown in Fig. 5.

Equation (2) indicates that  $v_d$  depends on  $n_{sh}$ , which is itself a function of temperature. In order to account for this,

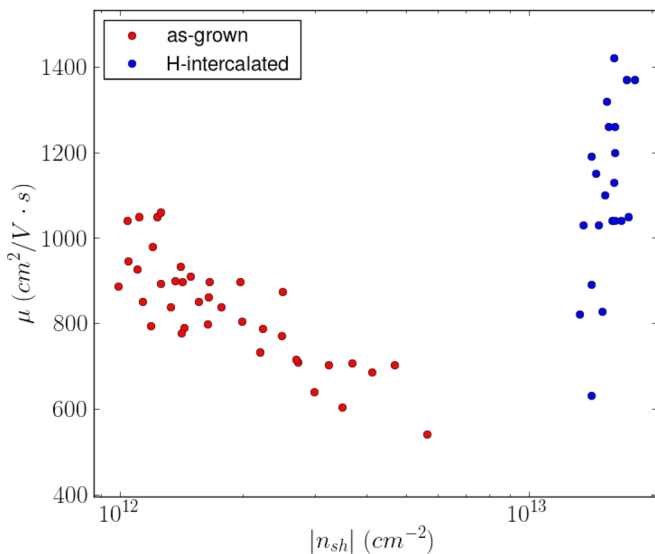


FIG. 5. A plot showing the measured carrier density versus Hall mobility.

the Fermi energy at 300 K is calculated for both materials given the carrier density  $n_{sh}(T = 300 \text{ K})$ . Assuming a Dirac cone model for the graphene band structure and non-degenerate Fermi-Dirac statistics, the Fermi level may be related to the carrier concentration via the Fermi Dirac integral<sup>18,19</sup>

$$n = N_g \int_0^{\infty} \frac{u}{1 + e^{u - \eta_f}} du, \quad (4)$$

$$p = N_g \int_0^{\infty} \frac{u}{1 + e^{u + \eta_f}} du.$$

The quantity  $N_g$  represents the effective sheet density of states and is given by the following relation:

$$N_g = \frac{g_s g_v}{2\pi} \left( \frac{k_b T}{\hbar v_f} \right)^2.$$

Here,  $g_s$  and  $g_v$  are the spin and valley degeneracies in graphene. Each carrier in graphene can have positive or negative spin polarization  $g_s = 2$ , such that each state can be occupied by two carriers with opposite spin polarization. In *monolayer* graphene, there are two inequivalent conical valleys in the first Brillouin zone ( $K$  and  $K'$ ) giving rise to a valley degeneracy  $g_v = 2$ . It should be noted that the valley degeneracy is higher for multilayer sheets of graphene. The variable  $\eta_f$  represents the Fermi energy  $E_f$  normalized to the thermal energy  $k_b T$  when the Dirac point  $E_D$  is taken to be zero energy. The exponential term evaluates to the following:

$$u \pm \eta_f = \frac{E \pm E_f}{k_b T}.$$

The variable of integration is thus energy normalized to thermal energy  $u = E/k_b T$ . These relations should be understood in conjunction with the energy-momentum dispersion relation in graphene:  $E - E_d = \hbar v_f |k|$ , where  $k$  is the wavenumber and  $v_f = 10^8 \text{ cm/s}$  is the Fermi velocity in graphene. Due to the high carrier concentration,  $E_f \approx \text{constant}$  over the measured temperature range. The Fermi level is found to be 250 meV for the as-grown material and 520 meV for the H-intercalated material. Given the Fermi level at  $T = 300 \text{ K}$ , it is possible to calculate carrier concentration as a function of temperature across the measured temperature range for both materials by Eq. (4) (Table I).

The electric field  $\mathcal{E}$  applied to the charge carrying sheet is calculated from dynamic IV measurements, TLM measurements of the contact resistance, and knowledge of the

TABLE I. A calculation of the sheet carrier concentration ( $\text{cm}^{-2}$ ) based on the measured data at 300 K for various temperatures. Values are normalized to  $10^{12} \text{ cm}^{-2}$ . The (+/-) indicates the sign of charge carriers for each material.

$10^{12} \text{ cm}^{-2}$	100 K	200 K	300 K
As-grown (-)	4.61	4.66	4.75
H-intercalated (+)	19.8	19.9	20.0

geometry of the sheet. For a given measurement, one can express the measured voltage  $V$  as a function of the measured current  $I$ , the contact resistance  $R_c$ , and the total microbridge resistance  $R_{mesa}$ . If the measured voltage drop and measured current are  $V$  and  $I$ , then by Ohm's law

$$V = I[2R_c + R_{mesa}]. \quad (5)$$

The voltage drop across the mesa is then

$$\begin{aligned} V_{mesa} &= V - 2IR_c \\ &= IR_{mesa}. \end{aligned}$$

Given the effective voltage drop across the mesa  $V_{mesa}$ , it is possible to calculate its sheet resistance  $R_{sh}$ . The width  $w$  of the mesa is generally not constant due to process accuracies such that  $w = w(l)$ . The mesa may be considered to be composed of an infinite number of series resistors with resistance  $dR_{mesa}$ . If the sheet resistance of the microbridge is assumed to be constant, the voltage drop across the mesa  $V_{mesa}$  may be calculated by integration.

$$V_{mesa} = IR_{sh} \int_0^{l_0} \frac{dl}{w(l)}. \quad (6)$$

The geometry of the patterned microbridge graphene mesas in Fig. 2 is approximated as shown in Fig. 6.

The solid lines represent the geometry which may be used for calculation. The rounded corners shown in dashed lines indicate the true geometry from photolithography. This approximation yields the following for the sheet resistance:

$$\begin{aligned} V_{mesa} &= IR_{sh} \cdot \\ &\left[ 4 \int_0^{l_{end}} \left[ w_{end} + \left( \frac{w_{end} - w_{ch}}{l_{end}} \right) l \right]^{-1} dl + \frac{l_{ch}}{w_{ch}} \right]. \end{aligned}$$

Carrying out the integration, one may solve for the mesa sheet resistance

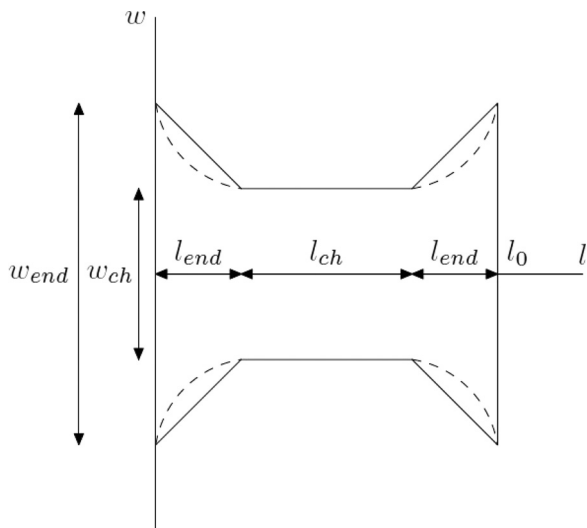


FIG. 6. The geometry assumed for the calculation of the sheet resistance given dynamic IV data. This should be compared with Fig. 2, which shows the true morphology of microbridge structures.

$$R_{sh} = R_{mesa} \left[ 2 \left( \frac{\log \left( \frac{w_{end}}{w_{ch}} \right)}{\tan \theta} \right) + \frac{l_{ch}}{w_{ch}} \right]^{-1}, \quad (7)$$

where

$$\tan \theta = \frac{2l_{end}}{w_{end} - w_{ch}}. \quad (8)$$

The term  $\theta$  is the current spreading angle describing the effect of the mesa geometry.<sup>5</sup> In the low field region, the dynamic IV characteristic is linear such that the differential sheet resistance is approximately constant.

$$R_{sh} = \frac{dV}{dI} \Big|_{V=0} = \text{constant}.$$

Using the above relations, it is possible to obtain  $R_{sh}$ . This value of  $R_{sh}$  may then be combined with Hall data in order to obtain the corresponding sheet carrier density  $n_{sh}$ . Finally, the carrier density may be combined with measured current and channel width giving the corresponding carrier velocity. The electric field may then be obtained by considering the voltage drop across the channel region.

$$R_{mesa} = 2R_{end} + R_{ch}. \quad (9)$$

The resistances associated with  $l_{end}$  and  $l_{ch}$  are denoted as  $R_{end}$  and  $R_{ch}$ , respectively. These resistances are obtained from Eq. (7). The magnitude of the electric field in the graphene bridge is

$$\mathcal{E} = \frac{V_0 - 2I_0[R_{end} + R_c]}{l_{ch}}. \quad (10)$$

Given dynamic IV data, measurements of the contact resistance, and Hall measurements, it is possible to obtain the velocity-field characteristic of a graphene microbridge. Accurate determination of the end geometry is critical, as it is found to have a non-negligible effect on the velocity-field extraction. The geometry is measured using SEM imaging.

#### IV. RESULTS

To model the velocity-field behaviour, the following empirical model is applied:<sup>4</sup>

$$v_d(\mathcal{E}) = \frac{\mu \mathcal{E}}{\left[ 1 + \left( \frac{\mu \mathcal{E}}{v_{sat}} \right)^\alpha \right]^{\frac{1}{2}}}. \quad (11)$$

Here,  $v_{sat}$  is the saturated electron velocity,  $\mu$  is the local mobility, and  $\alpha$  is a fitting parameter, which describes the rate of saturation. The electric field above which the electron velocity is saturating is given by  $\mathcal{E}_{sat} = v_{sat}/\mu$ .<sup>4</sup>

The effective mass of electrons and holes is approximately equal in graphene, such that similar values of  $\alpha$  for as-grown and H-intercalated material are expected.<sup>20</sup> The temperature dependent velocity-field data are fitted to Eq. (11) via a non-linear log-log least squares fit method. This gives  $v_{sat}$ ,  $\mu$ , and  $\alpha$  for each temperature. The measured

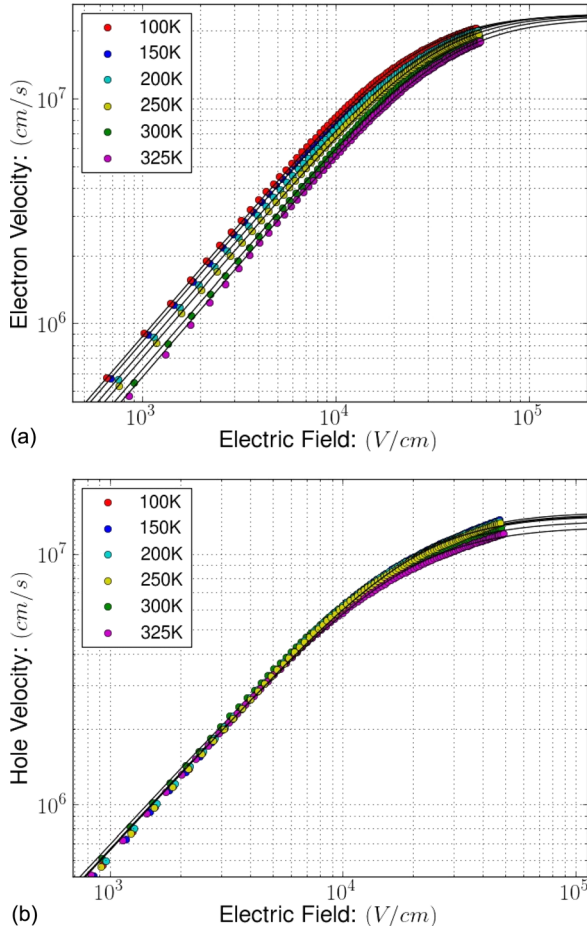


FIG. 7. Velocity-field plots with measured data and fitted data for various temperatures. Velocity-field curves are generated using an  $\alpha \approx 1.8$  model for as-grown material (top) and for H-intercalated material (bottom).

and modelled velocity-field curves for both materials and for temperatures ranging from 100 K to 325 K are shown in Fig. 7 (Table II).

The saturation field  $\mathcal{E}_{sat}$  for graphene is measured to be between that of silicon and SiC. For fields of magnitude below  $\mathcal{E}_{sat}$ , the velocity-field characteristic is linear and  $v_d \approx \mu\mathcal{E}$ .

## V. DISCUSSION

The extracted  $\mu$  and  $v_{sat}$  from the velocity-field measurements may be plotted as a function of temperature (Fig. 8). There are two dominant models for the temperature

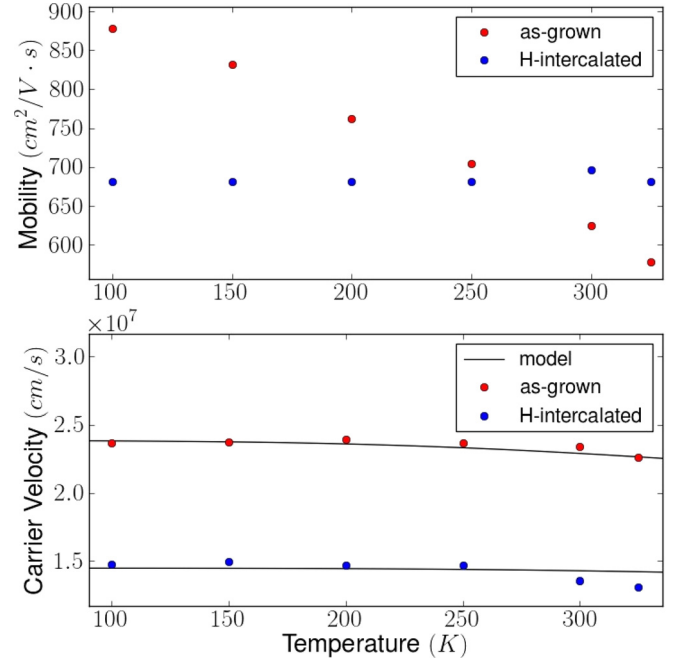


FIG. 8. The extracted mobility values as a function of temperature for the velocity-field curves for the as-grown sample shown in Fig. 7. The mobility is the slope of the velocity-field characteristic at low field. (Bottom) The extracted saturation velocity as a function of temperature for the velocity-field curves is shown for both the samples in Fig. 7. The trace represents the theoretical model for the temperature dependence of  $v_{sat}$  for the impurity scattering model (Eq. (12)).

dependence of the electron mobility  $\mu(T)$  in epitaxial graphene. First is a model in which the temperature dependence of carrier velocity is dominated by acoustic phonon scattering within the graphene. This model demonstrates a steep linear increase in the mobility for decreasing temperature.<sup>3,22</sup> There is also a constant mobility model ( $\mu(T) = const$ ) in which carrier velocity is determined by impurity scattering.<sup>8</sup> In reality, both acoustic phonon scattering and impurity scattering will occur such that the measured mobility should demonstrate characteristics of both models.

With the assumption of the impurity scattering model ( $\mu(T) \sim const$ ), it is possible to estimate the energy of the surface phonon  $E_{SO} = \hbar\omega_{SO}$  in 4H-SiC with the Illinois equation.<sup>8,23,24</sup>

$$v_{sat} = \frac{2}{\hbar} \frac{E_{SO}}{\pi\sqrt{\pi n}} \sqrt{1 - \frac{E_{SO}^2}{4\pi n(\hbar v_f)^2 N_{op} + 1}}. \quad (12)$$

TABLE II. A comparison of the parameters of the above fits to those of other well characterized materials at 300 K. The critical field is also reported indicating the field above which the electron velocity can be considered as saturated. Here,  $v_{sat}$  is reported in (cm/s),  $\mu$  in ( $\text{cm}^2/\text{s}$ ), and  $\mathcal{E}_{sat}$  in (kV/cm). The data for silicon correspond to n-type doping with a carrier concentration of  $n = 10^{17} - 10^{19} \text{ cm}^{-3}$ . The data for GaN correspond to n-type doping with a carrier concentration of  $n = 10^{17} - 10^{19} \text{ cm}^{-3}$ . The values reported for GaAs represent the peak electron velocity and corresponding electric field as GaAs demonstrates a velocity overshoot effect. Figures for GaN include measurements on AlGaIn/GaN heterostructures and bulk GaN substrates. These values also indicate the peak carrier velocity.

	As-grown	H-intercalated	4H-SiC <sup>5</sup>	AlGaIn/GaN <sup>21</sup>	GaN <sup>21</sup>	Si	GaAs <sup>7</sup>
$v_{sat}$	$2.3 \times 10^7$	$1.4 \times 10^7$	$1.6 \times 10^7$	$3.1 \times 10^7$	$2.5 \times 10^7$	$1.0 \times 10^7$	$2.1 \times 10^7$
$\mu$	630	700	130	430	250	1400	7500
$\mathcal{E}_{sat}$	37.0	19.4	123.7	72.0	100.0	7.1	2.8
$\alpha$	1.80	1.85	...	...	...	2.0	...

Here,  $N_{OP}$  represents the occupation statistics of the optical phonon mode in SiC for a given temperature. The phonon occupation  $N_{OP}$  is given by non-degenerate Bose-Einstein statistics.

$$N_{OP} = \frac{1}{e^{\frac{E_f}{kT}} - 1}. \quad (13)$$

Thus, as  $T$  increases,  $N_{OP}$  increases such that the number of optical phonons increases. Higher phonon densities increase the probability of scattering events between carriers and phonons. This has the effect of decreasing the saturation velocity,  $v_{sat}$ .

The expected temperature dependence for  $v_{sat}$  assuming the impurity scattering model (Eq. (12)) is shown in Fig. 8. By fitting the data to Eq. (12), it is possible to extract the surface phonon energy  $E_{SO} = \hbar\omega_{SO}$  for the 4H-SiC of 97 meV from the as-grown measurements and 115 meV from the H-intercalated measurements.

It is useful to describe these results in connection with the dielectric properties of the 4H-SiC substrate. The relative permittivity of a dielectric will vary with frequency  $\epsilon = \epsilon(\omega)$  in the following way:<sup>25</sup>

$$\epsilon(\omega) = \epsilon_{\infty} + \frac{\epsilon_0 - \epsilon_{\infty}}{1 - (\omega/\omega_{TO})^2}. \quad (14)$$

From the electrodynamic perspective, phonons are related to waves of electrostatic polarization, which exist in the presence of an oscillating electromagnetic field.

$$\mathbf{P}(\omega) = \epsilon_0[\epsilon(\omega) - 1]\mathbf{E}(\omega).$$

It can be shown that the frequencies of polarization waves in electrodynamic derivations may be related to the frequencies of phonon oscillations derived from lattice mechanics  $\omega_{TO}$  and  $\omega_{LO}$ .<sup>26</sup> In this way, optical phonons are directly related to dielectric properties arising from the polarizability of the substrate lattice.<sup>23</sup> The existence of optical surface phonons arises when one considers the form of the electric field at the boundary between a material with permittivity  $\epsilon(\omega)$  and vacuum  $\epsilon_{vac} = 1$ . Solving for the electromagnetic boundary equations in this problem gives the following dispersion relation:<sup>25-27</sup>

$$\omega^2(k) = \frac{1}{2}(\omega_k^2 + \omega_{LO}^2) - \frac{1}{2}\left[(\omega_k^2 + \omega_{LO}^2)^2 - 4\omega_k^2\omega_{SO}^2\right]^{\frac{1}{2}}.$$

Here the phonon frequencies  $\omega_{LO}$  and  $\omega_{SO}$  are the longitudinal optical and surface optical phonon frequencies. They can be expressed in terms of the dielectric constant of the material  $\epsilon$  and the transverse optical phonon frequency  $\omega_{TO}$ . Here,  $\omega_k = \sqrt{(\epsilon_{\infty} + 1)/\epsilon_{\infty}}ck$

$$\begin{aligned} \omega_{LO} &= \sqrt{\frac{\epsilon_0}{\epsilon_{\infty}}}\omega_{TO}, \\ \omega_{SO} &= \sqrt{\frac{\epsilon_0 + 1}{\epsilon_{\infty} + 1}}\omega_{TO}. \end{aligned} \quad (15)$$

TABLE III. A summary of the phonon energies for TO, SO, and LO modes in 4H-SiC. The first row indicates measurement by HREELS.<sup>28</sup> The second row indicates the measured SO energy from this work and the recalculated calculated TO and LO energies via Eq. (15) for the H-intercalated measurement. Energies are reported in meV.

4H-SiC	$\hbar\omega_{TO}$	$\hbar\omega_{SO}$	$\hbar\omega_{LO}$
HREELS	98.7	115.9	119.9
$v(\mathcal{E})$	96.5	115.0	117.6

Here,  $\epsilon_0$  is the static  $\omega = 0$  dielectric constant and  $\epsilon_{\infty}$  is the high frequency  $\omega \rightarrow \infty$  dielectric constant. The relation between  $\omega_{TO}$  and  $\omega_{LO}$  is known as the Lyddane-Sachs-Teller (LST) relation. From the above relations, it is clear that  $\omega_{TO} < \omega_{SO} < \omega_{LO}$  because  $\epsilon_0 > \epsilon_{\infty}$ . For 4H-SiC and 6H-SiC,<sup>28</sup>  $\epsilon_0 = \sqrt{\epsilon_{0,\perp}\epsilon_{0,\parallel}} = 9.812$  and  $\epsilon_{\infty} = \sqrt{\epsilon_{\infty,\perp}\epsilon_{\infty,\parallel}} = 6.609$ .<sup>28,29</sup> These calculations account for the anisotropy of  $\epsilon$  in the 4H-SiC and 6H-SiC polytypes. Table III summarizes the measurements of the phonon energies in 4H-SiC by high-resolution energy loss spectroscopy (HREELS) by Nienhaus *et al.* as well as our measurement of  $\hbar\omega_{SO}$  in the case of H-intercalated material.

The extracted value of  $\hbar\omega_{SO} = 115$  meV is reasonably close to the accepted value of 115.9 meV (Refs. 28 and 30) in the measurements on H-intercalated graphene. The H-intercalated result suggests that impurity scattering determines the transport properties. Furthermore, the transport properties of epitaxial graphene are strongly influenced by the substrate. Given that the mobility is constant in the H-intercalated measurement, it is reasonable that the H-intercalated material may be used to estimate the surface phonon energy in SiC in accordance with the impurity scattering model. The Fermi level in H-intercalated material is much higher than the phonon mode energy such that the temperature dependence in model is very weak. Furthermore, the hypothesis that H-intercalation somehow decouples graphene layers from the substrate must be considered alongside the observation that carriers in the H-intercalated graphene interact with substrate surface optical phonons.

The value obtained for as-grown graphene  $\hbar\omega_{SO} = 97$  meV in this measurement is non-physical based on Eq. (15). There are many potential reasons for this. The as-grown measurements demonstrate a weak linear increase in the mobility with decreasing temperature. This suggests that the transport properties in as-grown material are influenced by both acoustic phonon scattering and impurity scattering. In this way, the as-grown sample may be a poor candidate for estimating  $\hbar\omega_{SO}$  as such an estimation via Eq. (12) requires that  $\mu(T)$  is constant. Additionally, the influence of the buffer layer on transport properties in as-grown graphene is largely unknown. As-grown material also shows a much wider variation in the measured carrier density indicating that the epitaxial graphene layer is highly non-uniform. In the as-grown material, the Fermi level is lower, and the phonon coupling is stronger, giving a stronger dependence in the measured electron velocity with temperature.

The fundamental weakness in this method lies in the non-uniformity of epitaxial graphene, which produces statistical variation in the observed Hall data. This translates

directly into experimental error. Thus, it is necessary to examine the possibility of a more advanced structure design and processing strategy such that Hall measurements may be performed *in situ* with dynamic IV measurements.

## VI. CONCLUSIONS

A method of measuring the electron velocity in graphene mesas has been presented. The saturated electron drift velocity has been measured to be  $2.33 \times 10^7$  cm/s in as-grown epitaxial graphene and  $1.36 \times 10^7$  cm/s in H-intercalated epitaxial graphene. The extraction is performed by calculating the sheet resistance of microbridge structures based on measured data. From this value, one can infer the carrier concentration from Hall statistics gathered from a number of Van Der Pauw structures. The contact resistance is also measured and mesa geometry is considered. Temperature dependent measurements are used in order to extract an optical phonon energy for 4H-SiC assuming an impurity scattering model resulting in a measured surface phonon energy of  $E_{SO} \approx 115$  meV. This correlates well with the accepted value of  $\sim 115.9$  meV and seems to support an impurity scattering hypothesis. The direct corollary to this observation is that the transport properties of epitaxial graphene are strongly influenced by the substrate.

## ACKNOWLEDGMENTS

We acknowledge support from the Swedish Foundation for Strategic Research (SSF), the Knut och Alice Wallenberg Foundation (KAW), and European Science Foundation (ESF).

- <sup>1</sup>R. S. Shishir and D. K. Ferry, "Velocity saturation in intrinsic graphene," *J. Phys.: Condens. Matter* **21**(34), 344201 (2009).
- <sup>2</sup>A. Akturk and N. Goldsman, "Electron transport and full-band electron-phonon interactions in graphene," *J. Appl. Phys.* **103**(5), 053702 (2008).
- <sup>3</sup>D. K. Ferry, "Transport in graphene on bn and sic," in *2012 12th IEEE Conference on Nanotechnology (IEEE-NANO), August* (2012), pp. 1–5.
- <sup>4</sup>C. Canali, G. Majni, R. Minder, and G. Ottaviani, "Electron and hole drift velocity measurements in silicon and their empirical relation to electric field and temperature," *IEEE Trans. Electron Devices* **22**, 1045–1047 (1975).
- <sup>5</sup>I. A. Khan and J. A. Cooper, Jr., "Measurement of high-field electron transport in silicon carbide," *IEEE Trans. Electron Devices* **47**(2), 269–273 (2000).
- <sup>6</sup>V. E. Riginos, "Nonsaturating velocity-field characteristic of gallium arsenide experimentally determined from domain measurements," *J. Appl. Phys.* **45**(7), 2918–2922 (1974).
- <sup>7</sup>J. G. Ruch and G. S. Kino, "Measurement of the velocity-field characteristic of gallium arsenide," *Appl. Phys. Lett.* **10**(2), 40–42 (1967).
- <sup>8</sup>V. E. Dorgan, M.-H. Bae, and E. Pop, "Mobility and saturation velocity in graphene on sio[sub 2]," *Appl. Phys. Lett.* **97**(8), 082112 (2010).
- <sup>9</sup>K. I. Bolotin, K. J. Sikes, J. Hone, H. L. Stormer, and P. Kim, "Temperature-dependent transport in suspended graphene," *Phys. Rev. Lett.* **101**, 096802 (2008).
- <sup>10</sup>L. B. Biedermann, M. L. Bolen, M. A. Capano, D. Zemlyanov, and R. G. Reifengerger, "Insights into few-layer epitaxial graphene growth on 4h-SiC(0001) substrates from stm studies," *Phys. Rev. B* **79**, 125411 (2009).
- <sup>11</sup>A. Meyer, I. G. Ivanov, J. I. Flege, S. Watcharinyanon, J. Falta, L. I. Johansson, E. Janzen, J. Hassan, and C. Virojanadara, "Surface evolution of 4h-sic(0001) during in situ surface preparation and its influence on graphene properties," *Mater. Sci. Forum* **157**, 740–742 (2011).
- <sup>12</sup>C. Riedl, C. Coletti, T. Iwasaki, A. A. Zakharov, and U. Starke, "Quasi-free-standing epitaxial graphene on sic obtained by hydrogen intercalation," *Phys. Rev. Lett.* **103**, 246804 (2009).
- <sup>13</sup>M. Winters *et al.*, "A dc comparison study between h-intercalated and native epi-graphenes on sic substrates," *Mater. Sci. Forum* **740–742**, 129 (2013).
- <sup>14</sup>C. Coletti, K. V. Emtsev, A. A. Zakharov, T. Ouisse, D. Chaussende, and U. Starke, "Large area quasi-free standing monolayer graphene on 3c-sic(111)," *Appl. Phys. Lett.* **99**(8), 081904 (2011).
- <sup>15</sup>Y.-W. Tan, Y. Zhang, K. Bolotin, Y. Zhao, S. Adam, E. H. Hwang, S. Das Sarma, H. L. Stormer, and P. Kim, "Measurement of scattering rate and minimum conductivity in graphene," *Phys. Rev. Lett.* **99**, 246803 (2007).
- <sup>16</sup>G. Roelkens, D. Van Thourhout, and R. Baets, "Ultra-thin benzocyclobutene bonding of iii-v dies onto soi substrate," *Electron. Lett.* **41**(9), 561–562 (2005).
- <sup>17</sup>I. Angelov, H. Zirath, and N. Rosman, "A new empirical nonlinear model for hemt and mesfet devices," *IEEE Trans. Microwave Theory Tech.* **40**(12), 2258–2266 (1992).
- <sup>18</sup>T. Fang, A. Konar, H. Xing, and D. Jena, "Carrier statistics and quantum capacitance of graphene sheets and ribbons," *Appl. Phys. Lett.* **91**(9), 092109 (2007).
- <sup>19</sup>J. G. Champlain, "A first principles theoretical examination of graphene-based field effect transistors," *J. Appl. Phys.* **109**(8), 084515 (2011).
- <sup>20</sup>K. S. Novoselov, A. K. Geim, S. V. Morozov, D. Jiang, M. I. Katsnelson, I. V. Grigorieva, S. V. Dubonos, and A. A. Firsov, "Two-dimensional gas of massless Dirac fermions in graphene," *Nature* **438**, 197 (2005).
- <sup>21</sup>J. M. Barker, D. K. Ferry, D. D. Koleske, and R. J. Shul, "Bulk gan and algan/gan heterostructure drift velocity measurements and comparison to theoretical models," *J. Appl. Phys.* **97**(6), 063705 (2005).
- <sup>22</sup>E. H. Hwang and S. Das Sarma, "Acoustic phonon scattering limited carrier mobility in two-dimensional extrinsic graphene," *Phys. Rev. B* **77**, 115449 (2008).
- <sup>23</sup>M. V. Fischetti, D. A. Neumayer, and E. A. Cartier, "Effective electron mobility in si inversion layers in metal-oxide-semiconductor systems with a high-kappa insulator: The role of remote phonon scattering," *J. Appl. Phys.* **90**(9), 4587–4608 (2001).
- <sup>24</sup>I. Meric, M. Y. Han, A. F. Young, B. Ozyilmaz, P. Kim, and K. L. Shepard, "Current saturation in zero-bandgap, top-gated graphene field-effect transistors," *Nat. Nanotechnol.* **3**(11), 654–659 (2008).
- <sup>25</sup>S. Q. Wang and G. D. Mahan, "Electron scattering from surface excitations," *Phys. Rev. B* **6**, 4517–4524 (1972).
- <sup>26</sup>R. Fuchs and K. L. Kliewer, "Optical modes of vibration in an ionic crystal slab," *Phys. Rev.* **140**, A2076–A2088 (1965).
- <sup>27</sup>K. L. Kliewer and R. Fuchs, "Optical modes of vibration in an ionic crystal slab including retardation. I. Nonradiative region," *Phys. Rev.* **144**, 495–503 (1966).
- <sup>28</sup>H. Nienhaus, T. U. Kampen, and W. Monch, "Phonons in 3c-, 4h-, and 6h-sic," *Surf. Sci.* **324**(1), L328–L332 (1995).
- <sup>29</sup>A. A. Lucas and J. P. Vigneron, "Theory of electron energy loss spectroscopy from surfaces of anisotropic materials," *Solid State Commun.* **49**(4), 327–330 (1984).
- <sup>30</sup>A. Konar, T. Fang, and D. Jena, "Effect of high-k gate dielectrics on charge transport in graphene-based field effect transistors," *Phys. Rev. B* **82**, 115452 (2010).